

Quantum simulation of $(1 + 1)$ -dimensional $U(1)$ gauge-Higgs model on a lattice by cold Bose gases

Yoshihito Kuno¹, Shinya Sakane², Kenichi Kasamatsu², Ikuo Ichinose¹, and Tetsuo Matsui²

¹*Department of Applied Physics, Nagoya Institute of Technology, Nagoya, 466-8555, Japan and*

²*Department of Physics, Kindai University, Higashi-Osaka, 577-8502, Japan*

(Dated: August 8, 2018)

We present a theoretical study of quantum simulations of $(1 + 1)$ -dimensional $U(1)$ lattice gauge-Higgs models, which contain a compact $U(1)$ gauge field and a Higgs matter field, by using ultra-cold bosonic gases on a one-dimensional optical lattice. Starting from the extended Bose-Hubbard model with on-site and nearest-neighbor interactions, we derive the $U(1)$ lattice gauge-Higgs model as a low-energy effective theory. The derived gauge-Higgs model exhibits nontrivial phase transitions between confinement and Higgs phases, and we discuss the relation with the phase transition in the extended Bose-Hubbard model. Finally, we study real-time dynamics of an electric flux by the Gross-Pitaevskii equations and the truncated Wigner approximation. The dynamics is governed by a bosonic analog of the Schwinger mechanism, i.e., shielding of an electric flux by a condensation of Higgs fields, which occurs differently in the Higgs and the confinement phase. These results, together with the obtained phase diagrams, shall guide experimentalists in designing quantum simulations of the gauge-Higgs models by cold gases.

PACS numbers: 11.15.Ha, 67.85.Hj

I. INTRODUCTION

To understand physics of a given quantum many-body system in a coherent manner is not an easy matter. For example, the time development of these systems have not been clarified enough because high dimensionality of the state-vector space brings great difficulty for solving many-body Schrödinger equation [1]. The sign problem also prevents us from carrying out straightforward Monte Carlo simulations for models including fermionic matter fields [2].

In the last several years, as an alternative approach, quantum simulations of various quantum systems by using ultra-cold atomic gases on an optical lattice have attracted lots of interests [3]. This comes mainly from high controllability and versatility of such atomic systems. Quantum simulations of systems under a synthetic gauge field have already become feasible due to experimental developments [4]. Furthermore, recent studies have proposed several ideas for realizing simulators of quantum systems involving *dynamical gauge fields* [5]. Gauge systems appear in various fields of physics as an effective model, and to understand their dynamics is one of the most important problems. Also, proposals for an experimentally feasible atomic simulator of gauge systems still remain as an open problem.

In the previous papers [6–8], some of the present authors discussed how to simulate lattice gauge-Higgs models (GHMs) [9, 10] by bosonic atoms on a D -dimensional optical lattice ($D = 3$ in Refs. [6, 8] and $D = 2$ in Ref. [7]). The starting model in that approach is a cold atomic system described by the extended Bose-Hubbard model (EBHM) [11, 12]; a lattice model of bosons having both on-site and off-site interactions. The target gauge model, GHM, is a $U(1)$ lattice gauge theory [13] involving a compact $U(1)$ gauge field and a Higgs field in the

London limit. Reflecting the nonrelativistic nature of the EBHM, interactions in the GHMs are asymmetric in the space and time directions; some couplings in the spatial directions have no partners in the time direction in contrast to the lattice gauge theory considered in high-energy physics [13]. However, the GHMs have a very interesting phase diagram as we shall see, and quantum simulation of the GHMs is expected to give us a very useful insight on the dynamics of the gauge theory.

In this approach [6–8], the phase degree of freedom $\hat{\theta}_a$ of boson operator $\hat{\psi}_a = \exp(i\hat{\theta}_a)\sqrt{\rho_a}$ on the site a of the optical lattice plays the role of the compact $U(1)$ gauge field $\hat{\theta}_{r,i}$ defined on the link $(r, r + \hat{i})$ of a D -dimensional (spatial) lattice of lattice gauge theory ($i = 1, \dots, D$ is the direction index). Compared with the alternative approach called quantum link model (gauge magnet) [14], this approach has an advantage to express a compact $U(1)$ gauge theory in terms of the genuine $U(1)$ operator $\exp(i\hat{\theta}_{r,i})$ [15]. The Hamiltonian of the EBHM is known to contain an annoying term that breaks Gauss law of the pure gauge theory (i.e., theory containing no matter fields) and forces one to make a severe fine-tuning of its coefficient to generate a local gauge symmetry [5]. However, inclusion of the Higgs field converts this breaking term to a term expressing the genuine Gauss-law with Higgs charge and relieves us from the fine-tuning.

In this paper, we consider theoretically the atomic quantum simulation of the GHM with $D = 1$, supposing a system of Bosonic atoms on a one-dimensional (1D) optical lattice. This work is motivated by the following reasons:

(i) From experimental point of views, quantum simulation of gauge theories in a 1D spatial lattice is expected to be easier than that in higher-dimensional lattices [5]. The present approach is based on a set of single-component atoms with long-range interaction (e.g., dipole-dipole in-

teraction) loaded on a 1D optical lattice. It has the following advantages [15]; first, this set up is proved to be feasible experimentally [16]. Second, a digital quantum simulation of the Schwinger model has been realized recently by using a 1D chain of several sites of trapped ions [17]. In contrast, the present 1D optical lattice is scalable, i.e., hundreds of sites with large number of atoms can be prepared. Third, some approaches such as Ref. [18] use the quantum link model, whose realization requires two-component atoms on the optical lattice. The single-component atoms in the present approach is certainly more feasible in experiments.

(ii) We can expect nontrivial behavior of the phase transitions of the target GHM, not found in the higher-dimensional cases [6–8]. As shown later, the phase transition is governed by the Berezinskii-Kosterlitz-Thouless (BKT) type transition [19].

(iii) Non-equilibrium physics of the lattice gauge theories has not been deeply understood yet. This subject is closely related to the recent heavy-ion collision experiments in high-energy physics [20]. In our previous paper [7, 8], we applied the Gross-Pitaevskii (GP) model [21] to study the real time dynamics of an electric flux, showing that the dynamics qualitatively realizes the behavior expected in each phase of the GHM. On the other hand, since the quantum fluctuations become more important in 1D system, we should include some quantum correction to the GP approach. Actually, real-time dynamics of a lattice gauge model has been studied by tensor network method [22], which is mainly applicable for 1D quantum systems with low filling. Here, we use the truncated Wigner approximation [23] to study the effects of quantum fluctuations.

Let us explain the basic steps of the present paper. First, by applying the method in our previous papers [6–8] to the 1D EBHM *for large fillings of atoms* (large average occupation numbers of atoms per site) we obtain the (1+1)D GHM with short-range interactions. Here the additional +1D in the GHMs represents the imaginary-time axis in path-integral quantization for which we also use a lattice regularization. Next, we calculate the phase diagram of the derived GHM, which contains the Higgs phase and the confinement phase separated by the BKT transition. This phase diagram is compared with that of the EBHM to discuss the interesting relations between the strongly-correlated bosons and the gauge systems; namely, the Higgs phase corresponds to the superfluid phase and the confinement phase to Mott-insulator phase. This also provides an estimation of the relevant parameter region to simulate the phase transitions in experiments. Finally, we study the real-time dynamics of the GHM by using the GP equation [21] and the truncated Wigner approximation [23]. This mean-field approach naturally arises because of the assumption of the large fillings of atoms. Numerical results show that a prepared electric flux exhibits quite different behaviors depending on the Higgs or confinement phase. A phenomenon similar to the Schwinger mechanism is observed

numerically.

The paper is organized as follows. In Sec. II, we present a derivation from the experimentally realized model, the EBHM on the 1D optical lattice, to the target simulated model, the (1+1)D U(1) GHMs which follows our previous works [6, 8]. In Sec. III we discuss the phase diagram of the GHM calculated by the Monte Carlo simulations. The obtained phase diagram is compared with that of the EBHM, whose details of the calculation is described in Appendix A. In Sec. IV, we study non-equilibrium physics of the GHM, especially focusing on real-time dynamics of an electric flux. We present conclusion in Sec. V

II. RELATION BETWEEN THE EXTENDED BOSE-HUBBARD MODEL AND THE GAUGE-HIGGS MODEL

We start with the EBHM defined on a 1D optical lattice (see Fig. 1). The hamiltonian H_{EBH} is given as

$$H_{\text{EBH}} = \sum_a \left[-J(\hat{\psi}_a^\dagger \hat{\psi}_{a+1} + \hat{\psi}_{a+1}^\dagger \hat{\psi}_a) + \frac{U}{2} \hat{\rho}_a^2 + V \hat{\rho}_a \hat{\rho}_{a+1} \right], \quad (1)$$

where $\hat{\psi}_a^\dagger$ and $\hat{\psi}_a$ are creation and annihilation operators of bosonic atoms on the site a , respectively, satisfying $[\hat{\psi}_a, \hat{\psi}_{a'}^\dagger] = \delta_{aa'}$, etc. By representing $\hat{\psi}_\alpha = e^{i\theta_\alpha} \sqrt{\hat{\rho}_\alpha}$, we have the phase operator $\hat{\theta}_\alpha$ and the density operator $\hat{\rho}_\alpha$. The coefficient J represents the hopping strength, U the on-site interaction, and $V(> 0)$ the nearest-neighbor (NN) repulsive interaction generated by, e.g., a dipole-dipole interaction [24]. The above on-site repulsion $U(> 0)$ represents the sum of s -wave scattering interaction U_s and on-site dipole-dipole interaction U_d ; $U = U_s + U_d$. The s -wave scattering amplitude U_s is highly controllable by Feshbach resonance [25] and the hopping J is controlled by the strength of the laser that makes the optical lattice. On the other hand, the NN repulsion V is determined by the kind of the atoms loaded on the lattice and also depends on the lattice spacing. In particular, ratios J/U and V/U can become highly-controllable parameters in real experiments by changing lattice depth [3] and s -wave scattering lengths [25], respectively.

The procedure [6–8] to derive the GHM with local interactions from the EBHM for homogeneous density average at large fillings is based on a couple of assumption; (i) the average density is homogeneous and large, $\rho_{0a}(= \langle \hat{\rho}_a \rangle) = \rho_0 \gg 1$ (large filling) and (ii) the density fluctuation around ρ_0 is small. The point (ii) implies that we focus on the sector of low-energy excitations. Explicitly, we write the density operator as

$$\hat{\rho}_a = \rho_0 + \hat{\eta}_a, \quad (2)$$

and expand H_{EBH} with respect to the fluctuation operator $\hat{\eta}_a$ up to the second-order. This kind of expansion is widely used in atomic physics [3].

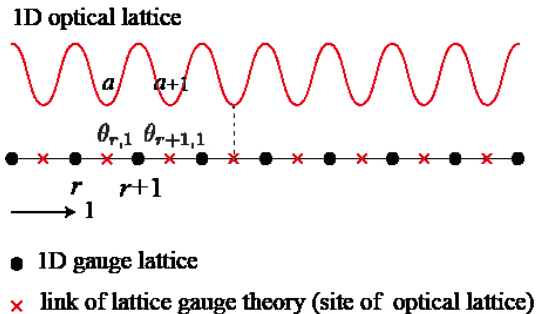


FIG. 1. (Color online) Optical and gauge lattices. Each site a of the optical lattice corresponds to a link of the gauge lattice as $a \leftrightarrow (r, r + 1)$. On the gauge link $(r, r + 1)$ sits the spatial component $\theta_{r,1}$ of gauge field.

To regard this expanded Hamiltonian as that of the GHM, we introduce a gauge lattice and a set of operators in gauge theory defined on it. The gauge lattice is the dual lattice of the optical lattice (see Fig. 1); the site r of the gauge lattice sits on the middle point of the link $(a, a + 1)$ of the optical lattice. We define the 1st component of the vector potential $\hat{\theta}_{r,1}$ and its conjugate momentum, namely the electric field \hat{E}_r , on the gauge link $(r, r + 1)$ as

$$\hat{\theta}_{r,1} = (-)^r \hat{\theta}_a, \quad \hat{E}_r = -(-)^r \hat{\eta}_a, \quad (3)$$

where we use the same character θ both for atomic and gauge variables (They can be distinguished by whether it carries the direction suffix 1). Strictly speaking, the electric field should carry the direction suffix 1 as $\hat{E}_{r,1}$, but we omit it in this paper because there are no other components in a 1D system. On the other hand, we keep the suffix 1 in $\hat{\theta}_{r,1}$ because we shall introduce the zeroth component of vector potential later [see $\theta_{x,0}$ in Eq. (10)]. These pairs satisfy the canonical commutation relations [13],

$$[\hat{E}_r, \hat{\theta}_{r',1}] = -i\delta_{rr'}, \quad [\hat{\eta}_a, \hat{\theta}_{a'}] = i\delta_{aa'}, \quad (4)$$

which come from the commutation relations of $\hat{\psi}_a$. The factor $(-)^r$ in Eq. (3) may look curious but is necessary to generate the Gauss law as we shall see. Then the expanded Hamiltonian up to $O(\eta^2) = O(E^2)$ is expressed

as

$$\begin{aligned} H_{\text{EBH}} &= C_{\rho_0} + H_{\text{GH}} + \Delta H + O(E^3), \\ C_{\rho_0} &= \left(\frac{U}{2} + V \right) \sum_r \rho_0^2, \\ H_{\text{GH}} &= \sum_r \left[\frac{V}{2} (E_{r+1} - E_r)^2 + \frac{g^2}{2} E_r^2 \right. \\ &\quad \left. - 2J\rho_0 \sum_r \cos(\theta_{r+1,1} + \theta_{r,1}) \right], \\ g^2 &= U - 2V, \\ \Delta H &= \frac{J}{4\rho_0} \sum_r (E_{r+1} + E_r)^2 \cos(\theta_{r+1,1} + \theta_{r,1}), \quad (5) \end{aligned}$$

where we omitted hat symbols for operators. There appear no terms linear in E_r because ρ_0 is chosen such that it gives rise to a stationary point of the energy. C_{ρ_0} is an irrelevant constant. The hopping J term of Eq. (1) generates both the last term of H_{GH} and the term ΔH . Their coefficients are $J\rho_0$ and J/ρ_0 respectively, and the latter is suppressed by an extra factor ρ_0^{-2} for large fillings. Therefore we neglect ΔH and keep H_{GH} as the Hamiltonian of the GHM for large fillings.

The first term of H_{GH} leads to Gaussian with respect to $\nabla_1 E_r \equiv E_{r+1} - E_r$, the divergence of the electric field, and gives rise to $\langle (\nabla_1 E_r)^2 \rangle \simeq V^{-1}$. This becomes the Gauss-law constraint $\nabla_1 E_r = 0$ for *pure gauge theory* in the limit $V \rightarrow \infty$, and this limit is just the fine tuning required for the pure gauge theory in Refs. [5]. After introduction of a Higgs field in the London limit, this term represents the genuine Gauss law ($\nabla_1 E_r = Q_{\text{Higgs}}$) with the Higgs charge Q_{Higgs} (see Ref. [8] for details).

The second term represents the energy of electric field. In the ordinary lattice gauge theory used in high-energy physics [13], its coefficient g^2 is the square of so called real gauge coupling constant g and g^2 is treated as positive definite. In our case, $g^2 = U - 2V$ may take *negative value* (although we used a suggestive notation g^2 that it may be positive). Here we can see that a homogeneous configuration of $\rho_{0a} = \rho_0$ is realized for $g^2 > 0$ by using a very simple type of the mean-field theory, i.e., two site mean-field theory. We take only two nearest-neighbor site of the Hamiltonian E_{EBH} , called even-site and odd-site. By putting a mean field ansatz $\psi_{\text{even}} \rightarrow \sqrt{\rho_{\text{even}}}$ and $\psi_{\text{odd}} \rightarrow \sqrt{\rho_{\text{odd}}}$ into the two sites, the EBHM mean field energy E_{EBH} , which depends on the two mean density is given as

$$E_{\text{EBH}} = -2J\sqrt{\rho_{\text{even}}\rho_{\text{odd}}} + \frac{U}{2}(\rho_{\text{even}}^2 + \rho_{\text{odd}}^2) + V\rho_{\text{even}}\rho_{\text{odd}} \quad (6)$$

Then by detecting the energy minimum under a canonical ensemble constraint, $\langle \rho_a \rangle = \rho_0$ ($\rho_{\text{even}} + \rho_{\text{odd}} = 2\rho_0$), we can show the homogeneity of the atom density. Fig. 2 indicates the homogeneity of the atom density in $(U-V)$ -plane. Here, we found that, ρ_{0a} is homogeneous for $g^2 >$

0, i.e., $\rho_{0a} = \rho_0$, while for $g^2 \ll 0$, ρ_{0a} takes an inhomogeneous DW configuration such as $\rho_{0a} = \rho_0 + (-)^a \delta\rho/2$ (see Fig. 2). Result in Fig. 2 also indicates the existence of a homogeneous ‘phase’ even for $g^2 < 0$. This comes from the fact that the ‘critical line’ $g^2 = U - 2V = 0$ is renormalized by the hopping J -term in H_{EBH} in Eq. (1). In Appendix A, we give rather detailed discussion on this homogeneous state and obtain the global phase diagram of the EBHM.

The third $J\rho_0$ term of H_{GH} expresses the NN coupling of the U(1) gauge field $U_{r,1} = \exp(i\theta_{r,1})$ as $J\rho_0 U_{r+1,1} U_{r,1} + \text{H.c.}$, but it breaks the gauge symmetry under $\theta_{r,1} \rightarrow \theta_{r,1} + \lambda_{r+1} - \lambda_r$ (λ_r is an arbitrary r -dependent real parameter) [13]. In Refs. [6–8] we introduced a U(1) Higgs field $\phi_r = \exp(i\varphi_r)$ in the London limit (its amplitude is frozen to unity) on the site r , and regard this term as a gauge-fixed version of the Higgs coupling to the unitary gauge $\phi_r = 1$ as

$$\begin{aligned} & -J\rho_0 \sum_r \phi_{r+2}^\dagger U_{r+1,1} U_{r,1} \phi_r + \text{H.c.} \\ \rightarrow & -J\rho_0 \sum_r U_{r+1,1} U_{r,1} + \text{H.c.} \end{aligned} \quad (7)$$

This Higgs coupling and the remaining terms in H_{GH} is invariant under the local U(1) gauge transformation [13]

$$\begin{aligned} U_{r,1} & \rightarrow U'_{r,1} = V_{r+1} U_{r,1} \bar{V}_r, \quad \phi_r \rightarrow \phi'_r = V_r \phi_r, \\ E_r & \rightarrow E'_r = E_r, \quad V_r \equiv \exp(i\lambda_r), \end{aligned} \quad (8)$$

where the bar symbol in \bar{V}_r denotes the complex conjugate. In short, $\hat{H}_{\text{GH}}(\phi, U, E) \equiv H_{\text{GH}}(\phi U \phi^\dagger, E)$ is a gauge-invariant Hamiltonian which we formally work with and the gauge invariant observables are calculable by its gauge fixed version $H_{\text{GH}}(U, E)$ of Eq. (5).

Here we comment that, in the present 1D system, the Gauss law term of gauge theory is to be supplied only by the U - and V -terms in H_{EBH} . This is in contrast with the higher dimensional [(2+1)D and (3+1)D] systems in which one must take additional next-NN interactions into account [7, 8]. This point shows that the 1D atomic system is more feasible to realize a quantum simulator in experiments than the higher dimensional systems.

To derive the gauge model, we start with the partition function $Z_{\text{GH}} = \text{Tr} \exp(-\beta \hat{H}_{\text{GH}}(\phi, U, E))$ defined from H_{GH} of Eq. (5) with the inverse temperature $\beta = 1/(k_{\text{B}}T)$ expressed in path-integral in canonical formalism (sum over canonical pair of coordinate and momentum). Then all the fields are defined on the (1+1)D lattice with its site denoted by $x = (x_0, x_1) \equiv (\tau, r)$ as $\phi_x, U_{x,1}, E_x$, where $\tau = 0, \dots, N-1$ is the site index along the imaginary-time axis discretized by the spacing $\Delta\tau \equiv \beta/N$ and we take the limit $N \rightarrow \infty$ formally. In this paper we omit the hat symbol in $\hat{\mu}$ ($\mu = 0, 1$) to denote the unit vector in the μ -th direction. Therefore $x+0$ and $x+1$ imply the NN site $(\tau+1, r)$ and $(\tau, r+1)$ respectively. We use ∇_μ as the forward difference operator $\nabla_\mu f_x \equiv f_{x+\mu} - f_x$.

We introduce the imaginary-time (τ) component of the gauge field $\theta_{x,0}$ on the link $(x, x+0)$ to make the first Gauss-law term of H_{GH} a linear form in $\nabla_1 E_x$, i.e.,

$$\begin{aligned} & \exp \left[-\Delta\tau \frac{V}{2} (E_{x+1} - E_x)^2 \right] \\ & = \int d\theta_{x,0} \exp \left[-\frac{1}{2V\Delta\tau} \theta_{x,0}^2 + i\theta_{x,0} \nabla_1 E_x \right]. \end{aligned} \quad (9)$$

Because every step in the approach of Refs. [6–8] is applied in the present (1+1)D system in a straightforward manner, we present the expressions for Z_{GH} as (For details see Sec. II of Ref. [8]),

$$\begin{aligned} Z_{\text{GH}} & = \int [d\theta_1][dE] \\ & \times \exp \left[\sum_\tau (iE_x(\theta_{x+0,1} - \theta_{x,1}) - \Delta\tau H_{\text{GH}}) \right] \\ & = \int [d\theta_0][d\theta_1][d\varphi] \exp(A_{\text{GH}}), \\ [d\theta_\mu] & = \prod_x \frac{d\theta_{x,\mu}}{2\pi}, \quad [d\varphi] = \prod_x \frac{d\varphi_x}{2\pi}, \quad [dE] = \prod_x \sum_{E_x=-\infty}^{\infty}. \end{aligned} \quad (10)$$

The action A_{GH} may be expressed in terms of the compact U(1) variables $U_{x,\mu} = \exp(i\theta_{x,\mu})$ on the link $(x, x+\mu)$, $\mu = 0, 1$ [$x = (x_0, x_1) = (\tau, r)$] and $\phi_x = \exp(i\varphi_x)$ as

$$\begin{aligned} A_{\text{GH}} & = A_{\text{I}} + A_{\text{P}} + A_{\text{H}}, \\ A_{\text{I}} & = \frac{c_1}{2} \sum_x \bar{\phi}_{x+0} U_{x,0} \phi_x + \text{c.c.}, \\ A_{\text{P}} & = \frac{c_2}{2} \sum_x \bar{U}_{x,0} \bar{U}_{x+0,1} U_{x+1,0} U_{x,1} + \text{c.c.}, \\ A_{\text{H}} & = \frac{c_3}{2} \sum_x \bar{\phi}_{x+2} U_{x+1,1} U_{x,1} \phi_x + \text{c.c.} \end{aligned} \quad (11)$$

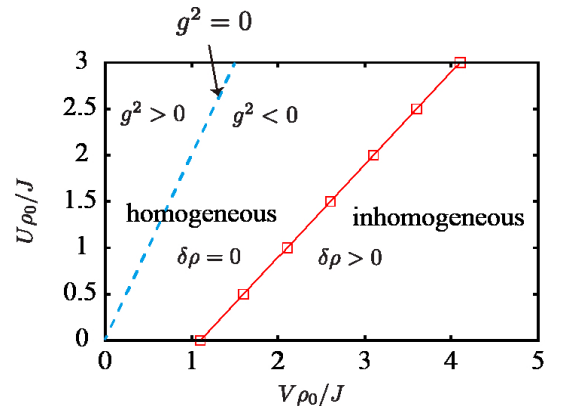


FIG. 2. (Color online) Mean-field result for the 1D ground-state configuration of the average density ρ_0 . It shows that the homogeneous configuration ($\delta\rho \equiv \rho_{\text{even}} - \rho_{\text{odd}} = 0$) is stable for $g^2 > 0$ as expected. However, a homogeneous state exists even for $g^2 < 0$ for moderate values of negative g^2 . The inhomogeneous configuration stands for the density-wave pattern ($\delta\rho > 0$). Detailed study on this point is given in Appendix A.

The parameters in A_{GH} are expressed in terms of those in H_{GH} and $\Delta\tau$ as

$$c_1 = \frac{1}{V\Delta\tau}, \quad c_2 = \frac{1}{g^2\Delta\tau}, \quad c_3 = 2J\Delta\tau\rho_0. \quad (12)$$

The action A_{GH} in Eq. (11) contains only the short-range interaction, and each term is obviously invariant under a *time-dependent local gauge transformation* [given by Eq. (8) with the replacement $r \rightarrow x = (\tau, r)$], and the term A_I is nothing but the gauge-invariant kinetic term of the Higgs field ϕ_x [9]. The present action (11) is derived from the nonrelativistic Hamiltonian (1) and has no relativistic invariance under change of directions $\mu = 0 \leftrightarrow \mu = 1$, which is in contrast with the conventional models [13] in lattice gauge theory. However, this model supports both the confinement and Higgs phases (see Sec. III) and therefore is interesting enough for simulation of the gauge theory.

III. PHASE DIAGRAM OF THE GHM

In this section we calculate the phase diagram of the GHM defined by Eqs.(10) and (11) by MC simulations. For ordinary second-order phase transitions, one may use the specific heat C_{GH} ,

$$C_{\text{GH}} = \frac{1}{L^2} \langle (A_{\text{GH}} - \langle A_{\text{GH}} \rangle)^2 \rangle, \quad (13)$$

to locate the transition point by the peak of C_{GH} . However, because the present GHM is a (1+1)D system with a global U(1) symmetry as we shall see, the general theorem allows neither second-order transition nor long-range order. One may expect, if any, a phase transition of the same type as the BKT transition that is well known in the 2D XY spin model [19]. This expectation is plausible because the original 1D EBHM itself is known to have a phase transition at zero temperature between the Mott-insulator and superfluid, where the superfluid has a quasi-long range order due to the low dimensionality of the space.

Let us summarize the 2D XY spin model and its BKT transition. Its action is given by

$$A_{\text{XY}} = J \sum_x \sum_{\mu=0,1} \vec{S}_{x+\mu} \vec{S}_x = J \sum_{x,\mu} \cos(\sigma_{x+\mu} - \sigma_x), \quad (14)$$

where $\sigma_x \in [0, 2\pi)$ is the XY spin angle defined on x and $\vec{S}_x \equiv (\cos \sigma_x, \sin \sigma_x)$. The BKT transition of the 2D XY model is of infinite order, signaled by divergence of the susceptibility χ ,

$$\chi \equiv \sum_y \langle \vec{S}_y \vec{S}_x \rangle = \sum_y \langle \cos(\sigma_y - \sigma_x) \rangle, \quad (15)$$

at the transition point $J = J_c \simeq 1.12$. This value deviates from the round peak of specific heat by $\sim 20\%$.

The spin-spin correlation function $G(x) \equiv \langle \vec{S}_x \vec{S}_0 \rangle$ for large $|x|$ behaves exponentially $\exp(-|x|/\xi)$ in the spin disordered ($J < J_c$) phase and algebraically $|x|^{-\eta}$ in the spin quasi-ordered ($J > J_c$) phase. The correlation length ξ and the critical exponent η depend on J as $\xi(J) \propto \exp(b/\sqrt{J_c - J})$ near J_c and $\eta(J_c) = 1/4$.

To locate the phase transition point, one may observe the scaling behavior of χ of Eq. (15) for lattice of size $L \times L$ with the periodic boundary condition. *In the quasi-ordered phase*, power decay of $G(x)$ gives rise to $\chi \propto L^{2-\eta(J)}$ for large L . One may define the scaled susceptibility density as $\bar{\chi}(J, \eta^*) \equiv L^{\eta^*-2} \chi(J)$ with arbitrary parameter η^* . Then one has

$$\bar{\chi}(J, \eta^*) \equiv L^{\eta^*-2} \chi(J) \propto L^{\eta^*-2} \times L^{2-\eta(J)} = L^{\eta^*-\eta(J)}. \quad (16)$$

Therefore, at $\eta^* = \eta(J)$, $\bar{\chi}(J, \eta(J)) \propto L^0$ becomes scale invariant (no L -dependence). We note that this scale invariance holds for every point of $J(> J_c)$. Among possible multiple set of scale-invariant points $(J, \eta(J))$, the smallest value of J is just the critical point J_c . On the other hand, *in the disordered phase*, behavior of $\chi(J)$ depends on the relation between L and ξ . For $L \gg \xi$ (i.e., J is well below J_c), the exponential decay of $G(x)$ gives rise to $\chi \propto \xi^2$ and $\bar{\chi}(J, \eta^*) \propto L^{\eta^*-2} \xi(J)^2$, which shows no scale-invariant points are possible (for $\eta^* \neq 2$). For other case ($L \lesssim \xi$), no explicit formula of $\chi(J)$ seems available. Although there is no analytic proof that $\bar{\chi}(J, \eta^*)$ has no scale invariant points throughout the disordered phase, we confirmed that it is the case by numerical analysis applying the same method to obtain Fig. 3(d).

Below we shall see a close relation between the GHM and the 2D XY model, and explore the possibility of a BKT-type phase transition of the GHM. Let us first consider the limit of $c_1 \rightarrow \infty$. Then A_I of Eq. (11) forces $U_{x,0} = 1$ [$\theta_{x,0} = 0 \pmod{2\pi}$] up to gauge rotation. By introducing the gauge-invariant angle variable σ_x (we use the same letter as the above XY spin angle) on the spatial link $(x, x+1)$ [i.e., between the site (x_0, x_1) and $(x_0, x_1 + 1)$] as

$$\sigma_x \equiv (-)^{x_1} (\varphi_x + \theta_{x,1} - \varphi_{x+1}), \quad (17)$$

A_{GH} reduces up to a constant to

$$A_{\text{GH}} \rightarrow c_2 \sum_x \cos(\sigma_{x+0} - \sigma_x) + c_3 \sum_x \cos(\sigma_{x+1} - \sigma_x). \quad (18)$$

This is just the action of the 2D XY spin model with the asymmetric couplings c_2 and c_3 . It has the global U(1) symmetry under $\sigma_x \rightarrow \sigma_x + \alpha$. This limiting model exhibits BKT transitions on a certain critical line in the c_2 - c_3 plane [26].

As c_1 is reduced from infinity, $\theta_{x,0}$ is allowed to fluctuate more. However, it is plausible to expect that the above critical line in the c_2 - c_3 plane survive for finite but large enough c_1 , and the BKT-type scaling relation (16) holds. Then, we determine the transition point $c_1 = c_{1c}$ for a given set of (c_2, c_3) using the scaled susceptibility density $\bar{\chi}$ of Eq. (16) calculated by A_{GHM} and Eq. (17).

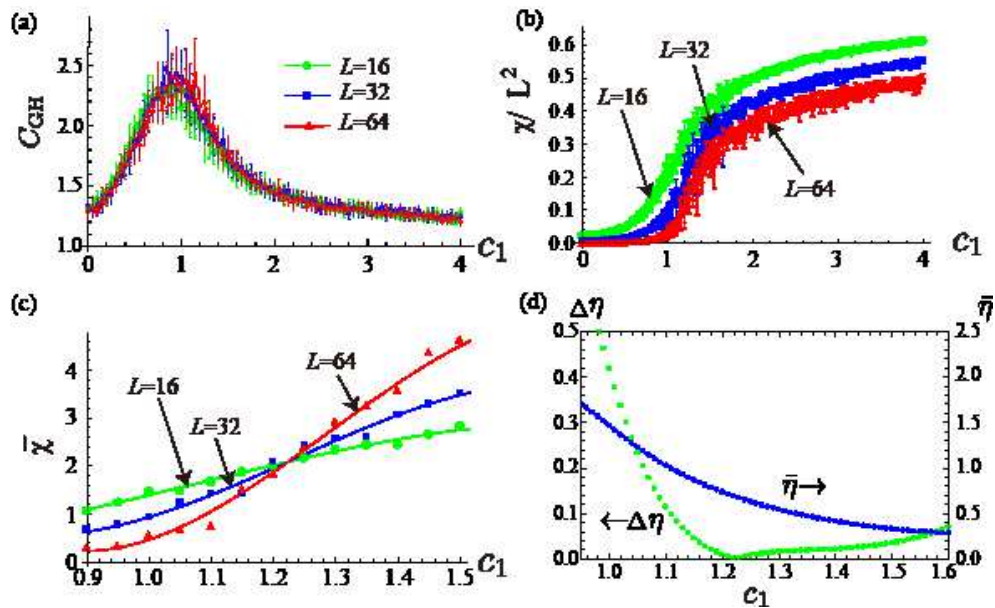


FIG. 3. (Color online) Thermodynamic quantities of the GHM of Eq. (10) and their scaling behavior for $c_2 = c_3 = 2.0$: (a) Specific heat C_{GH} of Eq. (13). (b) Susceptibility density χ/L^2 of Eq. (15). (c) Scaled susceptibility density $\bar{\chi}$ of Eq. (16) with the choice of critical values $c_1 = c_{1c} \sim 1.22$ and $\eta(c_{1c}) \sim 0.68$. These values are determined so that the three curves of $\bar{\chi}$ for $L = 16, 32, 64$ merge at a single point (see text). A large value of $\eta(c_{1c})$ reflects the fluctuations of $\theta_{x,0}$ in A_1 , which suppress the correlations among $\{\sigma_x\}$. (d) Average critical index $\eta(c_1)$ and deviation $\Delta\eta(c_1)$ from a triple intersection (see the text for their definitions). $\Delta\eta$ decreases as c_1 increases and reaches its minimum $\Delta\eta = 0$ at c_{1c} (three curves merge there) and keeps small values. Thus c_{1c} is interpreted as a BKT-type critical point dividing the disordered phase ($c_1 < c_{1c}$) and quasi-ordered phase ($c_1 > c_{1c}$) as Eq. (16) shows.

Explicit procedures are as follows;

- (i) Fix c_2 and c_3 and measure the susceptibility $\chi(c_1, L)$ along c_1 for three L 's (L_1, L_2, L_3).
- (ii) Obtain interpolating curves $y(c_1, L)$ for $\chi(c_1, L)$ in third-order polynomials in c_1 ;
- (iii) For $\bar{\chi}(c_1, \eta, L) = L^{\eta-2}y(c_1, L)$ (below we use η instead of η^* because no confusions may arise), set the conditions of a triple intersection; $\bar{\chi}(c_1, \eta, L_1) = \bar{\chi}(c_1, \eta, L_2) = \bar{\chi}(c_1, \eta, L_3)$, and solve these two equalities numerically.

From Eq. (16), one expects a continuous (multiple) set (c_1, η) of solutions for every value of c_1 starting at and larger than the critical value $c_1 = c_{1c}$.

In Fig. 3, we show (a) C_{GH} and (b) susceptibility density χ/L^2 for $c_2 = c_3 = 2.0$ and $L_1 = 16, L_2 = 32, L_3 = 64$. Instead of multiple set of solutions, we find a unique triple intersection at $c_1 = c_{1c} \simeq 1.22$ for $\eta \simeq 0.68$. In Fig. 3 (c) we show three $\bar{\chi}$ with this value. To understand the absence of multiple solutions, we introduce the distance $\Delta\eta$ from the triple intersection defined as follows; Each pair of three curves $\bar{\chi}(c_1, \eta, L)$ (e.g., L_a and L_b) with fixed c_1 has an intersection at $\eta = \eta_{ab}$. We define $\Delta\eta \equiv \text{Max of three distances, } |\eta_{ab} - \eta_{a'b'}|$. In Fig. 3 (d) we show $\Delta\eta$ together with the average of η , $\bar{\eta} \equiv (\eta_{12} + \eta_{23} + \eta_{31})/3$. The triple intersection at $c_1 = c_{1c}$ locates at the unique minimum of $\Delta\eta$ [$\Delta\eta(c_{1c}) = 0$] and separates the large $\Delta\eta$ -region ($c_1 < c_{1c}$) and the small $\Delta\eta$ -region ($c_{1c} < c_1$). By regarding $\Delta\eta$ in $c_{1c} < c_1$ al-

most vanishing, Eq. (16) tells us that the point $c_1 = c_{1c}$ is an approximate critical point of BKT-type phase transition separating the disordered phase ($c_1 < c_{1c}$) and the quasi-ordered phase ($c_{1c} \leq c_1$). Slow but steady development of $\Delta\eta$ from zero with increasing $c_1 (> c_{1c})$ shows that there exist some corrections to the power-law decay of spin correlations. One may account for it by finite-size effect generally; in particular, by the logarithmic corrections [27] that may become relatively important for smaller η . Then, we expect that $\Delta\eta$ for $c_1 > c_{1c}$ tends to small if we use the data obtained for systems with larger L . To calculate the critical point for general (c_2, c_3) below, we repeat to identify a unique triple intersection (scale-invariant point) as the BKT-type critical point. This manipulation is supported because a quite similar behavior of $\Delta\eta(J)$ is observed for the 2D XY model giving rise to $J_c \sim 1.11(1.12), \eta(J_c) \sim 0.23(0.25)$ in good agreement with the known results in parentheses for larger L .

In Fig. 4, we show the phase diagram in the $(c_1 c_3 - c_2 c_3)$ plane obtained in the same procedure as in Fig. 3 (c). The four transition lines correspond to $c_3 = 0.5, 1.0, 2.0$ and 3.0 . The two coordinates $c_1 c_3$ and $c_2 c_3$ of this plane are chosen so that they are dimensionless and $\Delta\tau$ independent combinations (see Sec. III of Ref. [8] for detailed discussion on this point). We note that there are no transitions in the region of $c_1 c_3 \lesssim 1.4$ because the data fitting in the form of Eq. (16) failed there. This is consistent

with our assumption that finite but sufficiently large c_1 is a necessary condition for BKT-type transition.

Because the disordered phase necessarily realizes for small c_1, c_2, c_3 's, the lower (smaller $c_2 c_3$) region in Fig. 4 corresponds to the disordered phase, and the higher (larger $c_2 c_3$) region corresponds to the quasi-ordered phase. In gauge theory, typical and well-known phases are Higgs, confinement, and Coulomb phases. The magnitude $\Delta\theta$ of fluctuations of gauge field $\theta_{x,\mu}$ increases in this order [9, 13, 28]. The magnitude ΔE of fluctuations of conjugate electric field E_x decreases in this order due to the uncertainty principle. Because we have two phases in Fig. 4, we naturally identify the spin-disorder phase as the confinement phase and the quasi-ordered phase as the Higgs phase. This is supported by the phase diagrams obtained for related GHMs derived from the 2D and 3D EBHM [6–8].

In order to identify the relevant parameter regions in experiments, it is important to compare the phase diagram of Fig. 4 to that of the original EBHM Eq. (1). In Fig. 5, we show the phase diagram of the EBHM in small V/J regime, which is obtained by the MC simulations in Appendix A. There are two phases. In the Mott insulator (MI) phase, the strong on-site repulsion U stabilizes the uniform distribution of atoms without the phase coherence. For the large hopping J , the superfluid (SF) forms as a result of the Bose-Einstein condensation. In Fig. 5, the red dotted line shows the phase boundary of the EBHM between the MI and the SF, which was determined by a scaling method. For details, see Appendix A and Fig. A.1. To compare the phase diagrams of BHM and GHMs, we transport critical lines shown in Fig. 4 to those in the $(U/J\rho_0 - V/J\rho_0)$ plane of Fig. 5, by using the relations between the parameters such as $c_1 c_3 = 2(V/(J\rho_0))^{-1}$ and $c_2 c_3 = 2(J\rho_0)/(U - 2V)$. The phase boundaries of the two models are fairly in good agreement for $g^2 > 0$ and this result certifies the existence the confinement-Higgs phase transition.

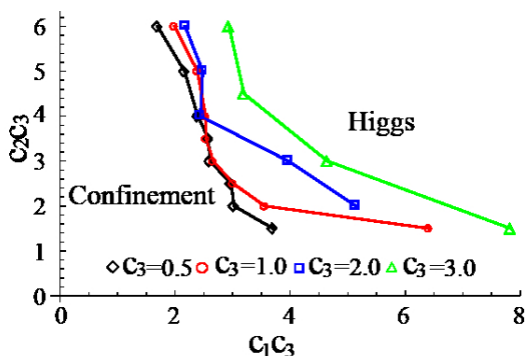


FIG. 4. (Color online) Phase diagram of the short-range GHM of Eq. (10) (corresponding to EBHM for homogeneous large fillings) obtained by the path-integral MC simulation. In the Higgs phase, fluctuations of gauge field $\Delta\theta$ is small, while, in the confinement phase, $\Delta\theta$ is large and fluctuations of the electric field ΔE is small.

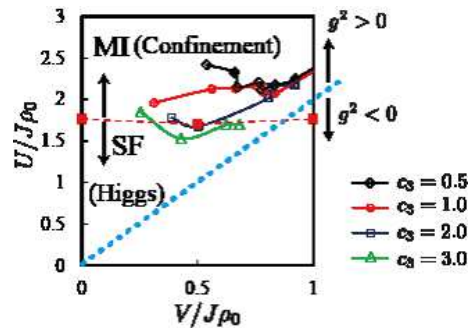


FIG. 5. (Color online) Phase diagram obtained by the path-integral MC simulations for $L=16, 32,$ and 64 , where L^2 is size of the space-time lattice. There are two phases, SF (superfluid) and MI (Mott insulator). We show the gauge-theoretical interpretation of each phase. Experimental setup with the parameter regions labeled ‘Higgs’ and ‘confinement’ are suitable for an atomic quantum simulation of the $U(1)$ GHMs. The blue broken line represents the vanishing gauge coupling, $g^2 (\equiv U - 2V) = 0$. The red dotted line is the phase boundary obtained in Appendix A.2. From the view point of the gauge theory, for $g^2 > 0$ and large U the ground state is confinement phase, in which the system has no phase coherence, whereas for $g^2 > 0$ and small U the ground state is Higgs phase, in which the system has strong phase coherence, i.e., SF phase.

In other words, our target phases are the MI phase and the SF phase in relatively small V regime; the two phases in cold atomic system has explicit meaning of the lattice gauge theory. Fig. 5 also shows suitable parameter regions for the quantum-simulation experiment on the GHM. This fact certainly supports that the confinement-Higgs phase transition can be observed by experiments of ultra-cold atoms in a 1D optical lattice.

The phase diagram of the BHM in large V regime itself has various interesting phases [29, 30]. As the NN repulsion is getting larger compared to the on-site repulsion, the assumption of uniform density configuration $\hat{\rho}_a \rightarrow \rho_0$ is broken, and the density wave phase appears in the phase diagram, in which an imbalance in the density at the even and odd sites exists. The result of the MC simulation for large V is also given in Appendix A.

IV. REAL-TIME DYNAMICS OF ELECTRIC FLUX STRING

In the high-energy physics, study of non-equilibrium dynamics of the gauge theories in Minkowski space-time has been a challenging problem. Its detailed study is going to be even more important inspired by recent heavy-ion collision experiments [20]. In this section, we study real-time dynamics of an electric flux in the Higgs and confinement phases observed by the path-integral MC simulations in Sec. III. To this end, we employ the GP equation, which is a reliable method to simulate dynamical behavior of a condensed fluid in condensed matter

physics especially for the superfluid behavior [31]. In general the GP equation is suitable for the SF (Higgs) phase, however in this section we extend the limitation, i.e., apply the GP equation to the MI (confinement) phase and focus on investigating qualitative behavior of both phases. A similar problem of real-time dynamics of an electric flux was addressed in an atomic quantum simulation of the Schwinger model, the (1+1)D quantum electrodynamics (QED), in Refs. [22, 32], where the tensor network simulation was used. Interestingly enough, the calculations in Refs. [22, 32] report qualitatively different behavior of the electric flux depending on values of the gauge coupling and mass of the electron.

From Sec. III, the present (1 + 1)D GHMs have two different phases, the Higgs and the confinement phases, therefore study of dynamical behavior of the electric flux gives important and interesting insight into the gauge dynamics in each phase. A similar problem for the higher-dimensional cases has been already addressed in our previous work [7, 8], where we have obtained qualitative difference of flux string behavior for each phases. In the present (1 + 1)D case, the direct comparison between the GHM in Eq. (5) and the Schwinger model is possible for the string dynamics.

The GP equation can be derived from the coherent path-integral of the EBHM as a saddle point equation. When the Lagrangian L is described as $L = -\sum_a i\psi_a^*(d\psi_a/dt) - H_{\text{EBH}}$, the Euler-Lagrangian equation $\delta L/\delta\psi_a^* = 0$ becomes the GP equation. From this procedure, the GP equation for the EBHM is given by

$$i\frac{1}{J}\frac{\partial\psi_a}{\partial t} = -(\psi_{a-1} + \psi_{a+1}) + \frac{U}{J}\rho_a\psi_a + \frac{V}{J}(\rho_{a-1} + \rho_{a+1})\psi_a + \frac{\mu'}{J}\psi_a, \quad (19)$$

where we have added chemical potential term $\mu'\psi_a$ by which the average density $\langle|\psi_0|^2\rangle = (1/N)\sum_a|\psi_a|^2 = \rho_0$ is controlled. In what follows, we set the equilibrium density $\rho_0 = 1$ by putting $\mu' = \rho_0(U + 2V) - 2J$. Here it should be remarked that this is a kind of the normalization and results for other densities can be obtained by a simple rescaling as $\psi_a \rightarrow \sqrt{\rho_0}\psi_a$ with $(U, V) \rightarrow \frac{1}{\rho_0}(U, V)$. A system of 200 spatial lattice sites with the free boundary condition is used and the time step Δt for the numerical calculation is set as $\Delta t = 10^{-4}$. The time scale $t = 1$ is ~ 0.32 [msec] by using the energy scale $U/h \sim 500$ [Hz] in typical experiments. In Eq. (19), the dissipation term is not included, and therefore the total energy is conserved during the time evolution.

As an example of a non-equilibrium state of the system, we consider the state with a single electric flux with a length R , i.e., we set the electric flux string in the initial state and solve the GP equation numerically. Hereafter we use the gauge lattice label, $a \rightarrow (r, 1)$. Explicitly, we set the initial configuration as $|\psi_{r,1}|^2 = [1 + (-1)^r(0.1)]\rho_0$ for $r_1 - R \leq r \leq r_1 + R - 1$ (r_1 is the center of the string). On the other sites, $|\psi_{r,1}|^2 = \rho_0$. In experiments the above initial flux is created by the density modulation

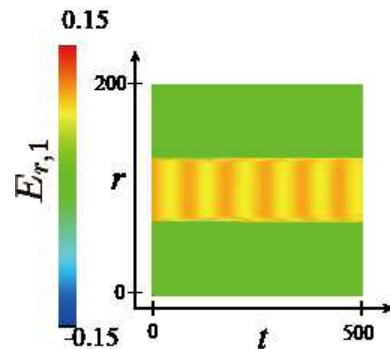


FIG. 6. Solution of the GP equation (19) for $U/J = 10^3$, $V/J = 1.0$ and $g^2/J = 0.2$. An electric flux string is stable because effect of the Higgs field is negligibly small.

[33]. In our numerical simulation, we set the length of the electric flux $R = 60$. In the confinement phase, this length is expected to be long enough for observing the typical quark-confinement phenomena [28, 34].

We first briefly consider the case of sufficiently small J , and verify that the electric flux string is stable by solving the GP equation (19). In our numerical simulation, the electric field E_r are defined as

$$E_r \equiv (-1)^r(|\psi_{r,1}|^2 - \rho_0). \quad (20)$$

This corresponds to a density fluctuation from mean density. The typical numerical results is shown in Fig. 6. When J is very small, the effects of the Higgs field is very small and the system has properties of the pure compact U(1) gauge theory.

In Fig. 7 (b)-(d), we show the time development of an electric flux along line $g^2/J = 0.2$ in the phase diagram. The results show that from the Higgs phase to the confinement phase, the stability of the electric flux is increased. In fact, there is a striking difference between the Higgs phase and the confinement phase; in the Higgs phase the electric flux spreads out. On the other hand in the confinement phase, the form of the initial flux does not change. In addition, we find that in both phases an oscillation of the electric field in the flux takes place. This behavior of the flux string means that a pair production of the Higgs particle and the resultant string breaking takes place. But in the confinement phase the restoration of the flux string readily occurs as a result of the strong gauge coupling. By contrast, in the Higgs phase the initial electric flux is unstable, i.e., bits of electric flux appear and they spread out from the initial region $r_1 - R \leq r \leq r_1 + R - 1$. This behavior comes from the condensation of the Higgs field and the resultant spontaneous symmetry breaking of the global U(1) gauge symmetry, i.e., the charge is not conserved in the Higgs phase.

In order to evaluate the spread of the electric field from the initial string, we measure the mean value of electric field strength $\langle E^2 \rangle_{\text{out}}$ outside of the initial place of the

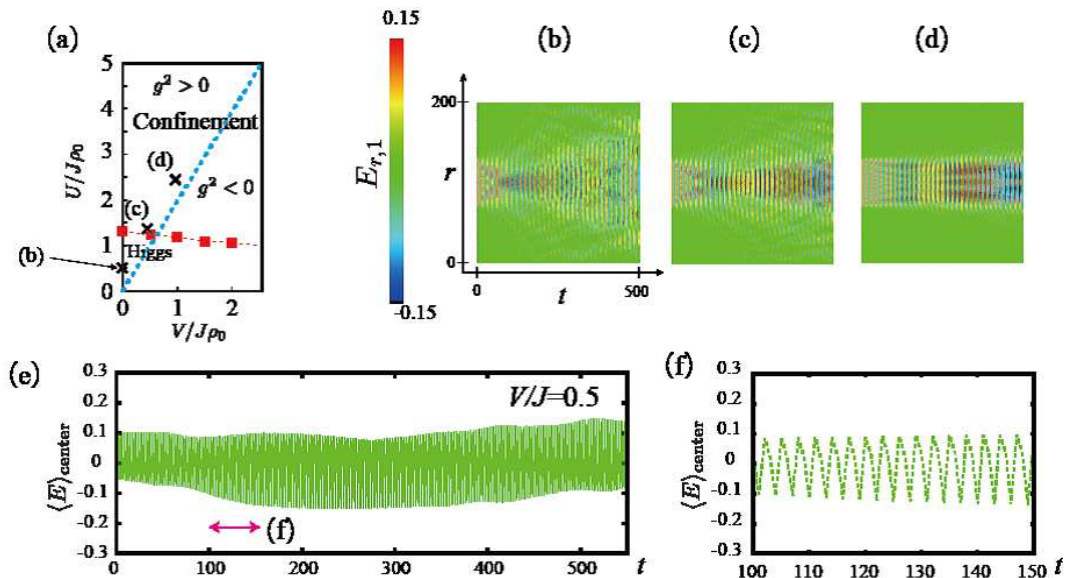


FIG. 7. (Color online) Real time-dynamics of a single electric flux. (a): Global phase diagram of the EBHM by the path-integral MC. (See Appendix A and Fig. A.1). The black crosses in the phase diagram indicate the locations on which the string dynamics is observed as in the right panels (b)-(d). (b)-(d): The time evolution of a single electric flux of length $R = 60$ in $L = 200$ lattice. All time evolutions have the same gauge coupling $g^2/J = 0.2$. For $V/J = 0$ (b) and $V/J = 0.5$ (c), the initial electric flux gradually spreads out along the time evolution and the pure-gauge Gauss law, $\text{div}E = 0$, does not work. For $V/J = 1$ (d), the shape of the initial electric flux is not broken. This indicates that the pure-gauge Gauss law works for the initial flux. For all cases (b)-(d), the electric fields oscillates changing their sign. This phenomenon is explained by the string-antistring oscillation that is also observed in the QED real-time simulation in Ref. [22, 32]. (e) and (f): For the case (c), the electric field averaged over the central ten sites, $\langle E \rangle_{\text{center}}$. The oscillation period is ~ 3.1 [kHz] in our time scale and the period depends only on the value of J .

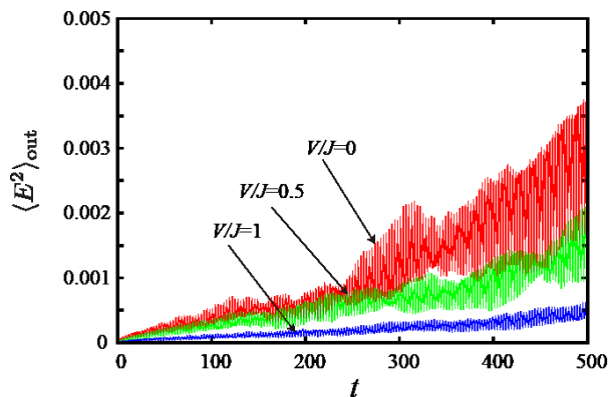


FIG. 8. (Color online) Mean value of electric field per link out of the initial electric flux, $\langle E^2 \rangle_{\text{out}}$. As decreasing of the value of V , the electric field spreads out of its initial string position. $g^2/J = 0.2$.

electric flux,

$$\langle E^2 \rangle_{\text{out}} \equiv \frac{1}{L-R} \sum_{(r,1) \notin \text{string line}} E_r^2. \quad (21)$$

Fig. 8 shows the $\langle E^2 \rangle_{\text{out}}$ for some typical values of the Gauss-law coupling V along the line $g^2/J = 0.2$. It is ob-

vious that as the value of V decreases, $\langle E^2 \rangle_{\text{out}}$ increases rapidly as a function of time, i.e., the initial configuration of the electric flux is unstable, and electric-field excitations propagate out of the initial electric flux.

In addition, Fig. 7 exhibits another remarkable behavior of the electric field as non-equilibrium phenomena. The results show that on the sites, where the initial electric flux exists, the electric fields are oscillating and changing their sign in both the Higgs and the confinement phases. The data in Fig. 7 (e) and (f) shows the time evolution of the electric field averaged over the central ten sites $\langle E \rangle_{\text{center}}$. Similar behavior was observed in all three cases; the central electric field in all cases oscillates in time and takes even negative values. The result is similar to behavior of an electric flux in Schwinger model with a small electron mass as reported in Refs. [22, 32], and the phenomenon is called the string-antistring oscillation. Quantum link version of QED was also studied from this point of view [35]. All the above studies indicate that the pair creation takes place in the central region of the electric flux as the Schwinger mechanism tells [36]. The two initial static charges residing on the edges of the initial electric flux tend to be shielded by particles of opposite charge. The initial electric flux vanishes as a result. After that, the reverse process happens, i.e., the pair creation recurs and the electric flux in the opposite direction is created. Iterating this process

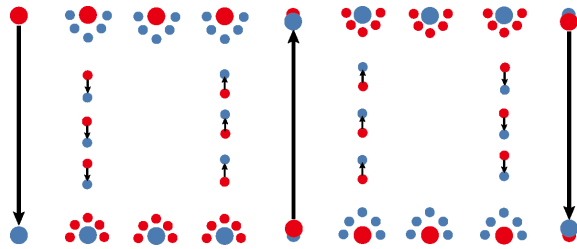


FIG. 9. (Color online) Schematic picture of string-antistring oscillation. This phenomenon comes from the Schwinger mechanism that was first suggested for QED [36]. The red circle represents a positive charge particle and the blue one is negative charge particle. The black arrow represents an electric flux tube between a pair of opposite static charges.

causes consequently the string-antistring oscillation. Our results in Figs.7 (b)-(f) for the U(1) GHM suggest that a similar string-antistring oscillation process takes place as in QED. Fig. 9 illustrates schematically the string-antistring oscillation process.

In the above, we studied the real-time dynamics of the electric flux string by using the GP equation. Results concerning to the Higgs phase are reliable as the Higgs phase is nothing but the SF and the order parameter ψ_a has only small fluctuations there. On the other hand, one may think that use of the GP equation for the MI regime is not appropriate even in the region close to the phase boundary to the SF. However, we expect that our study for the weak MI regime captures at least qualitatively correct picture of the string dynamics. In fact, the numerical results presented above are very similar to those obtained by other numerical results for closely related gauge models in Refs. [22, 32].

Anyway, a more detailed study of the dynamics of the flux string in the confinement-MI regime is important and it gives some useful remarks on the experimental setup. To this end, the idea of the truncated Wigner approximation (TWA) is useful [23], that is, we simulate the real-time dynamics of the flux string with different initial conditions. In the above, on solving the GP equation, we employed the initial condition such that the phase of the wave function $\theta_{r,1} = 0$. However in the MI state, the phase of the ‘condensate’ fluctuates as a result of the uncertainty relation between the particle number and the phase. In other words, the fluctuations of the phase cannot be avoided in the MI even if a prominent experimental technique to control the phase of the ‘condensate’ is used. This fact arises questions about the reliability of the results obtained by the GP equation.

Here, to study the effect of the phase fluctuation, we employ the initial condition such that $\theta_{r,1} = \lambda_r \pi$ and solve the GP equation, where the variables $\{\lambda_r\}$ are homogeneously distributed random numbers between $[-\Delta_m, \Delta_m]$ with $\Delta_m > 0$. To calculate the physical quantities like the density at each site, we take 100 samples, which have different initial conditions produced by the random numbers $\{\lambda_r\}$, and take average of the cal-

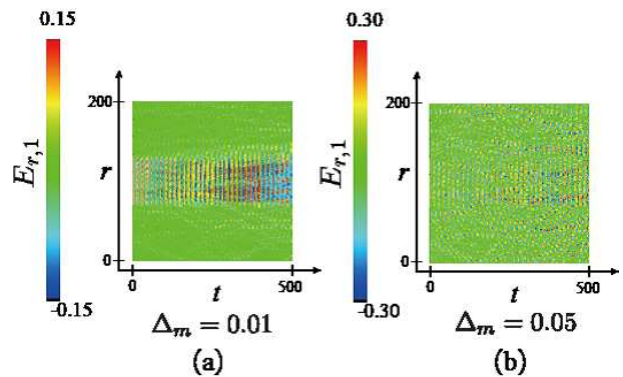


FIG. 10. (Color online) Real-time dynamics of the flux string in the confinement region with random distributions of the wave-function phase in the initial condition. These results were obtained by averaging 100 samples with different initial phase distribution. For $\Delta_m = 0.01$, the stable evolution of the string is observed, whereas for $\Delta_m = 0.05$, only small portion of the initial string configuration remains.

culated quantities over the samples. In this way, we obtain results of the real-time dynamics of the electric flux. This sampling method essentially corresponds to the TWA [23].

Fig. 10 shows the real-time dynamics of the flux string for the parameters $V/J = 1$, $U/J = 2.2$, which locates in the weak MI region in the phase diagram, and for two cases of the random distribution of the phase, $\Delta_m = 0.01$ and 0.05 . The other conditions are the same with those in the previous calculation. For $\Delta_m = 0.01$, the stable evolution of the string is observed, whereas for $\Delta_m = 0.05$, only small portion of the initial string configuration remains. From the above result and the uncertainty relation of the number and phase, $\Delta n \cdot \Delta \theta \geq \frac{1}{2}$, the fluctuation of the atomic number Δn at the initial state is required as $\Delta n \gtrsim 1/(0.05 \cdot 2\pi) \sim 3.2$. To satisfy this requirement in experiments, the average particle number must be sufficiently large and also a sufficient number modulation in the flux string is needed. If this condition is satisfied, the string-antistring oscillation in Fig. 7 is to be observed. More detailed study on this problem by using the full TWA and its extension [23] will be reported in a future publication.

Finally let us comment on the real-time dynamics of the flux string in the confinement-MI region apart from the phase boundary to the SF. In this region, the GP equation is not applicable, as the phase of the ‘condensate’ fluctuates rather strongly. However, this region corresponds to the strong-coupling region of the GHM, and therefore the string tension of the electric flux is strong. Then it is naturally expected that the string is quite stable and its fluctuations in time are small, and as a result its electric field is kept positive, $E_r > 0$. In fact, this phenomenon was observed in the numerical study of the gauge models in Refs. [22, 32].

TABLE I. Correspondence between the phases of EBHM and GHM. $\Delta\theta$ is the magnitude of fluctuations of atomic phase θ_a (vector potential $\theta_{r,1}$).

EBHM	U(1) GHM	$\Delta\theta$	$\rho_{0a} \equiv \langle \hat{\psi}_a \rangle$
MI	Confinement	large	ρ_0 (homogeneous)
SF	Higgs	small	ρ_0 (homogeneous)

V. CONCLUSION

We explained how to realize the atomic quantum simulation of the (1+1)D GHM by using cold atomic gases on the optical lattice. By means of the path-integral MC simulations, we obtained the phase diagrams of the GHM and also the EBHM at large filling and verified that these two phase diagrams are in good agreement with each other for the parameter region of the positive gauge coupling. We examined the phases of the EBHM from the gauge-theoretical point of view and the result is summarized in Table I.

By using the GP equations for the EBHM, we investigated dynamical properties of the electric flux put on a line as an initial state. In the confinement region of the GHM, the string breaking and restoration of the electric flux is observed, which has similar properties to the Schwinger mechanism in QED. On the other hand in the Higgs region, the flux spreads out and many bits of electric flux develop. Finally we discussed the reliability of the results obtained by the GP equations by using the idea of the TWA, and gave some remarks for the experimental setup to observe the string-antistring oscillation. We hope that the above phenomena will be observed experimentally in the near future. In particular, dynamical behavior of the transition from the confinement to Higgs phases is quite interesting and expected to be observed by the strong controllability and the versatility of the cold atomic system.

Finally, let us note that our approach identifies the phase and the amplitude of atomic variable as U(1) vector potential and the electric field respectively, and introduce the Higgs field to relax the crucial fine tuning to realize the Gauss' law. These general and universal procedures make us possible to define corresponding GHMs of wide variety both for high and low fillings and also for homogeneous and inhomogeneous atomic distributions. Although this GHM may contain nonlocal interactions in some cases and look quite different from the conventional lattice gauge theory, it is important that GHM is of course a "gauge theory having gauge symmetry". It obviously opens the way to study gauge theory in more general view points. Also such gauge-theoretical view points may shed some lights backward on studying the original atomic systems as partly shown in Sec. A 3.

ACKNOWLEDGMENTS

Y. K. acknowledges the support of a Grant-in-Aid for JSPS Fellows (No.JP15J07370). This work was partially supported by Grant-in-Aid for Scientific Research from Japan Society for the Promotion of Science under Grant No.JP26400246, JP26400371 and JP26400412.

Appendix A: Global phase diagram of extended Bose-Hubbard model in the $(V/J - U/J)$ plane for large fillings

In this Appendix, we study the global phase diagram of the 1D EBHM in the *whole* $(V/J - U/J)$ -plane at large fillings by taking account of both *homogeneous and inhomogeneous local density average* $\rho_{0a} \equiv \langle \hat{\rho}_a \rangle$. To this end, we first derive an effective model, which is to be used for study of the EBHM in the whole parameter region in the $(V/J - U/J)$ -plane, in particular even for a negative g^2 . This model includes the local variational density introduced in Ref. [37] in addition to the spatial vector potential $\theta_{x,1}$, and is capable to cover the case of inhomogeneous local density average for $g^2 \ll 0$ right region of Fig. 2. This model is complement to the gauge-theoretical study of the EBHM for $g^2 > 0$ in Sec. II as we explain later on. In this Appendix, we also show the results of MC simulation of this effective model, and compare the result with that of Sec. III.

1. Effective model for homogeneous and inhomogeneous local density with large fillings

In contrast to Eq.(2), we consider a general (a -dependent) local density average ρ_{0a} small fluctuations around it by writing

$$\hat{\rho}_a = \rho_{0a} + \hat{\eta}_a. \quad (\text{A.1})$$

To derive the effective model, we expand H_{EBH} with respect to $\hat{\eta}_a$ up to $O(\hat{\eta}^2)$ and discard the term like ΔH in Eq. (5) to obtain

$$\begin{aligned} H_{\text{EBH}} &= H_{\rho_{0a}} + H' + O(\eta^3), \\ H_{\rho_{0a}} &= \sum_a \left[\frac{U}{2} \rho_{0a}^2 + V \rho_{0a} \rho_{0,a+1} - \mu \rho_{0a} \right], \\ H' &= \sum_a \left[\frac{V}{2} (\eta_{a+1} + \eta_a)^2 + \frac{g^2}{2} \eta_a^2 \right. \\ &\quad \left. - 2J \sqrt{\rho_{0,a+1} \rho_{0a}} \cos(\theta_{a+1} - \theta_a) \right], \end{aligned} \quad (\text{A.2})$$

where the suffices a of the variables refer to sites in the optical lattice. We have included the chemical-potential term in the last term of $H_{\rho_{0a}}$ to fix the average total particle number $\langle \sum_a \hat{\rho}_a \rangle = \sum_a \rho_{0a} = L \rho_0$. Because we treat $\{\rho_{0a}\}$ as the variational parameters, the partition

function $Z_{\text{EBH}} = \text{Tr} \exp(-\beta H_{\text{EBH}})$ is expressed as

$$Z_{\text{EBH}} = \text{Max} Z_{\rho}(\{\rho_{0a}\}),$$

$$Z_{\rho}(\{\rho_{0a}\}) = \int [d\eta][d\theta] \exp \left[\sum_{a,\tau} (-i\eta_a \nabla_0 \theta_a - \Delta\tau H_{\text{EBH}}) \right], \quad (\text{A.3})$$

where the symbol ‘Max’ in the first line indicates to find the maximum value with respect to the parameters $\{\rho_{0a}\}$. (For details, see Ref. [37].) As in Sec. II, all the fields *except* ρ_{0a} are defined on the (1+1)D lattice with the site (τ, a) as $\eta_a(\tau), \theta_a(\tau)$ (the argument on τ in these fields is omitted) and $\nabla_0 \theta_a \equiv \theta_a(\tau+1) - \theta_a(\tau)$.

First, we consider the case of $g^2 < 0$. As we see in Sec. II, the density fluctuations η_a in H' of Eq. (A.2) become unstable for $g^2 < 0$. This *instability* is related to the appearance of phase such as the DW. However as the mean-field theory in Sec. II shows, the condition $g^2 < 0$ does not necessarily give the DW phase due to the effect of the hopping term. Therefore, more careful study is required for the case $g^2 < 0$.

Returning to the original EBHM, *higher-order terms of η_a appear in the potential from the hopping term, which prefers the homogeneity of the system.* This is the origin of the ‘homogeneous phase’ between the region $g^2 > 0$ and the inhomogeneous region shown in Fig. 2. Then, let us see what happens if the higher-order terms of η_a up to $O(\eta^4)$ are taken into account. The potential energy $V(\eta)$ for a configuration $\eta_a = (-)^a \eta$ has the following form,

$$V(\eta) = \alpha g^2 \eta^2 + \lambda \eta^4 \quad (\alpha, \lambda > 0)$$

$$= \lambda (\eta^2 - \xi^2)^2,$$

$$\xi \equiv \sqrt{\frac{-\alpha g^2}{2\lambda}} \quad (> 0 \text{ for } g^2 < 0), \quad (\text{A.4})$$

where η^3 -term is deleted by the optimal choice of $\{\rho_{0a}\}$ and we put $\theta_{a+1} = \theta_a$ to minimize the hopping term in the Hamiltonian as we are mostly interested in the phase boundary of the SF. The potential $V(\eta)$ has a double-well shape for $g^2 < 0$ and the potential minima are given at $\eta_a = \pm\xi$; where $\xi(> 0)$ is a certain number that depends on the parameters J, U, V and ρ_0 . The above observation suggests an approximation that one takes only those two configurations $\eta_a = \pm\xi$ into account instead of integrating over $\eta_a \in (-\infty, \infty)$ [38]. If the amplitude of the fluctuation ξ is (sufficiently) small, the homogeneous configuration is realized, which occurs for moderate values of U, V , and negative $g^2 = (U - 2V)$ [39]. Here, it should be remarked that *this ‘phase’ is reminiscent of the Haldane insulator* [29, 30], which is observed for the EBHM at low fillings, although the non-local string order does not exist in the present case.

To perform the η -integration in the path integral, we make further approximation by factorizing integrations over $\{\eta_a\}$ ’s to the product of single-site integrals over each η_a . This implies that we neglect correlations among $\{\eta_a\}$ described by the NN interactions of the V and J terms in H' of Eq. (A.2). By using these approximations,

we evaluate Z_{ρ} in Eq. (A.3) for the case of $g^2 < 0$ as follows;

$$Z_{\rho} = \int [d\theta] Z_{\theta} \exp \left[-2J\Delta\tau \sum_{a,\tau} \sqrt{\rho_{0,a+1}\rho_{0a}} \cos(\theta_{a+1} - \theta_a) \right],$$

$$Z_{\theta} = \int [d\eta] \exp \left[\Delta\tau \sum_{a,\tau} \left(-i\eta_a \nabla_0 \theta_a - \frac{g^2}{2} \eta_a^2 + D_4(\eta^4) \right) \right]$$

$$\simeq \prod_{a,\tau} [\exp(i\Delta\tau \xi \nabla_0 \theta_a) + \exp(-i\Delta\tau \xi \nabla_0 \theta_a)]$$

$$\simeq \exp \left[-\frac{1}{2} \sum_{a,\tau} (\xi \Delta\tau)^2 (\nabla_0 \theta_a)^2 \right]$$

$$\simeq \exp \left[\sum_{a,\tau} (\xi \Delta\tau)^2 \cos(\nabla_0 \theta_a) \right], \quad (\text{A.5})$$

where $D_4(\eta^4)$ refers to the term of $O(\eta^4)$, which was used to obtain Eq. (A.4). The approximate expression for Z_{θ} is the result discussed above, and we have incorporated the compactness of θ_a in the final expression.

From Eq. (A.5), an effective theory of the EBHM for the case $g^2 < 0$, which we call Z_{ρ}^{E} , is derived as in the previous discussion in Sec. II,

$$Z_{\text{EBH}}^{\text{E}} = \text{Max} Z_{\rho}^{\text{E}}(\{\rho_{0a}\}),$$

$$Z_{\rho}^{\text{E}}(\{\rho_{0a}\}) = \int \prod [d\theta] \exp(A_{\text{eff}} - \Delta\tau H_{\rho_{0a}}), \quad (\text{A.6})$$

$$A_{\text{eff}} = \sum_{a,\tau} \left[C_{\tau} \cos \nabla_0 \theta_a + 2J\Delta\tau \sqrt{\rho_{0,a+1}\rho_{0a}} \cos(\nabla_1 \theta_a) \right],$$

where the parameter C_{τ} is given as $C_{\tau} = 2(\xi \Delta\tau)^2$ from Eq. (A.5) for the case $g^2 < 0$. The above model defined by Eq. (A.6) is the effective theory, which is used for study on the global phase diagram of the EBHM as we discuss below.

Let us consider *the case $g^2 > 0$* . As we shall see, the effective model Z_{ρ}^{E} in Eq. (A.6) can be also used to calculate the phase diagram for $g^2 > 0$ if the constant C_{τ} is suitably chosen. This is because A_{eff} in Eq. (A.6) has the same structure with A_{GH} of Eq. (11) in the unitary gauge $\phi_x = 1$ for *small* V . In fact, A_{I} in Eq. (11) squeezes $\theta_{x,0} \rightarrow 0 \pmod{2\pi}$ for $V \rightarrow 0$. Then, A_{P} reduces to the C_{τ} -term in Eq. (A.6) [To make comparison, we recall the relation $\theta_{x=(\tau,r),1} = (-)^r \theta_{a,1}(\tau)$]. A_{H} reduces to the second term of Eq. (A.6) with homogeneous ρ_{0a} which is preferred by H_{ρ_0} for small V . Namely, two system coincide with the following relations;

$$A_{\text{P}} \rightarrow c_2 \cos(\nabla_0 \theta_{a,1}) \leftrightarrow C_{\tau} \cos(\nabla_0 \theta_{a,1}),$$

$$A_{\text{H}} \rightarrow c_3 \cos(\nabla_1 \theta_{a,1}) \leftrightarrow 2J\Delta\tau \rho_0 \cos(\nabla_1 \theta_{a,1}),$$

$$C_{\tau} = c_2 \equiv \frac{1}{g^2 \Delta\tau} \simeq \frac{1}{U \Delta\tau}, \quad c_3 = 2J\Delta\tau \rho_0, \quad (\text{A.7})$$

where the last relation is the same as Eq. (12).

Finally for sufficiently large $V(> U \gg J)$, the effective theory in Eq. (A.6) correctly predicts the existence of the

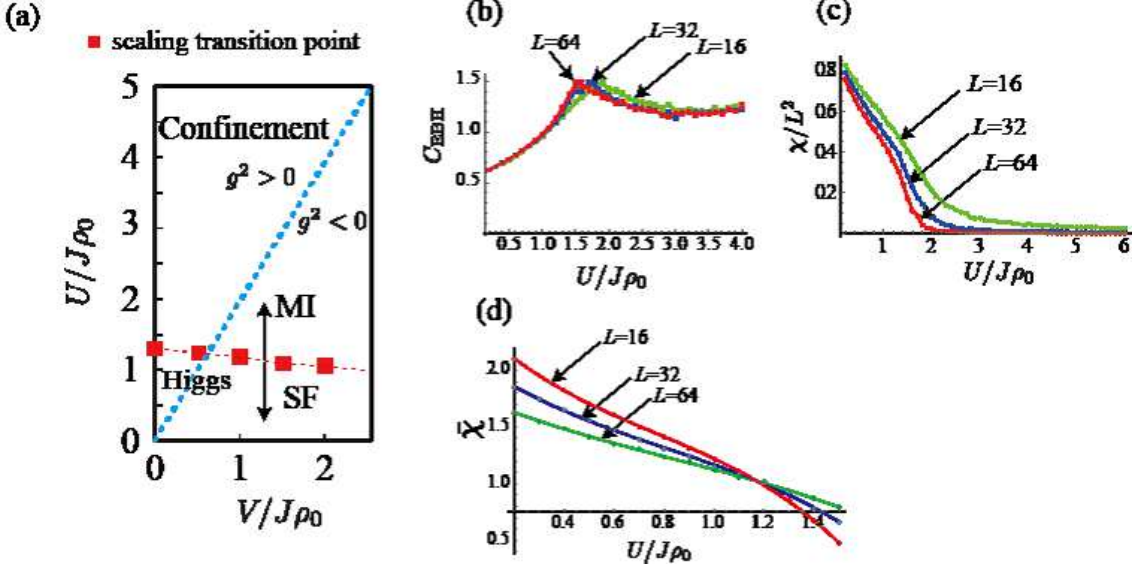


FIG. A.1. (Color online) (a) Phase diagram of the effective model in Eq.(A.6) obtained by the MC simulations. This MC calculation includes the update of the variational parameter $\{\rho_{0a}\}$. The phase boundaries determined by the scaling of $\chi = \sum_{\ell} G_B(\ell)$. (b) Specific heat C_{EBH} for $V/J = 1$. (c) Susceptibility density χ/L^2 in three different lattice size $L = 16, 32$ and 64 . (d) Scaled susceptibility density $\bar{\chi} = L^{\eta-2}\chi$. To determine the detailed phase boundary of the SF phase, we use $\bar{\chi}$. By choosing the exponent η and U/J suitably, we found that three curves of $\bar{\chi}$ merge at a point, which is the transition point (see Sec. III). Through this analysis, we verified that the SF-MI transition is a BKT-type phase transition. For $V/J = \rho_0$, the critical point is $U/J \sim 1.17\rho_0$ and the exponent is $\eta \sim 0.24$. MC simulation of the effective model in Eq.(A.6) under-estimates the SF in the vicinity $g^2 \approx 0$ as explained in the text.

DW. In fact for this parameter region, $H_{\rho_{0a}}$ in Eq. (A.6) is dominant, which favors the DW state, i.e., the state with $\rho_{0a} = \rho_0 + (-)^a \delta\rho/2$, as the ground-state. The other terms related to the quantum fluctuations θ_a are irrelevant to the formation of the DW whose existence is governed by the variational slow variables $\{\rho_{0a}\}$.

Here, we should remark on the applicability of the effective model Eq. (A.6). In the discussion for the case $g^2 < 0$, we simply put $\eta_a = \pm\xi$ on the integration over η_a . Also for the case $g^2 > 0$, only in the region $U \gg V$, A_{eff} coincides with A_{GH} , in which the effects of the NN repulsion (i.e., the V -term) are taken into account properly. Therefore, A_{eff} in Eq. (A.6) is not applicable for the region $g^2 \approx 0$ although the MC study of it gives suggestive results in that region as, $\{\rho_{0a}\}$ are treated as variational parameters in A_{eff} . See the results in the following subsection.

In conclusion, the considerations in this subsection support to use the model defined by Eq. (A.6) to study the EBMH.

2. Global phase diagram in the $(V/J - U/J)$ -plane for large fillings

In this subsection we calculate the global phase diagram in the $(V/J - U/J)$ -plane of the 1D EBHM for large fillings by performing MC simulation of the effective theory of Eq.(A.6).

In the practical calculation, we put $\Delta\tau = 1$, and the global average ρ_0 as the unit. We also put $C_\tau = 1/U$ as the on-site repulsion hinders the SF. This manipulation may underestimate the region of the SF in the phase diagram since in certain parameter region of $g^2 \approx 0$, fairly large density fluctuations exist and as a result, the enhancement of the SF may take place [40]. Phase boundaries are determined by calculating ‘‘internal energy’’ U_{EBH} and ‘‘specific heat’’ C_{EBH} defined by

$$U_{\text{EBH}} = -\frac{1}{L^2}\langle A_\tau \rangle, \quad (\text{A.8})$$

$$C_{\text{EBH}} = \frac{1}{L^2}\langle (A_\tau - \langle A_\tau \rangle)^2 \rangle. \quad (\text{A.9})$$

$$A_\tau = A_{\text{eff}} - \Delta\tau H_{\rho_{0a}},$$

where the above quantities are calculated using the effective model Eq.(A.6). We also use the boson correlation

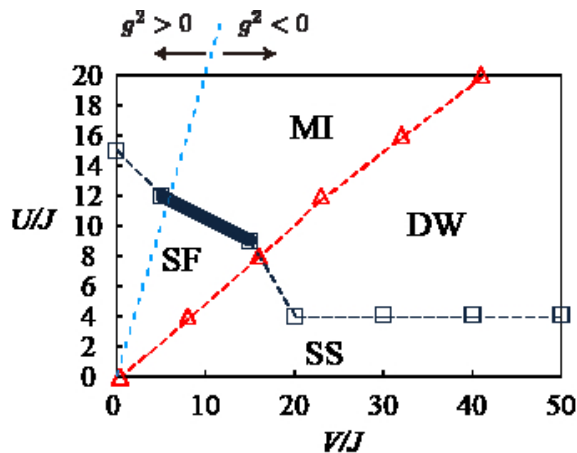


FIG. A.2. (Color online) Phase diagram of the effective model in Eq.(A.6) obtained by the MC simulations for $L=16$. Average filling is 10 per site ($\rho_0 = 10$) and we employed canonical ensemble. This MC calculation *includes the update of the variational parameter* $\{\rho_{0a}\}$. The target regime is large V . The specific regime of the phase boundary between SF and MI, $5 \lesssim V/J \lesssim 10$ is not clear.

function $G_\psi(\ell)$ and the DW correlation function $G_\rho(\ell)$ defined by

$$G_\psi = \langle \cos(\theta_{a+\ell} - \theta_a) \rangle, \\ G_\rho = (-1)^\ell \langle (\rho_{0,a+\ell} - \rho_0)(\rho_{0a} - \rho_0) \rangle, \quad (\text{A.10})$$

to identify the phases.

We employed the standard Metropolis algorithm [41] with the local update as before. *To begin with, we fix the variational parameters*, i.e., employ the assumption of homogeneous density $\rho_{0a} = \rho_0$. This manipulation corresponds to the London limit for a U(1) Higgs field $\phi_r = \exp(i\varphi_r)$ in Sec. II. In small V ($0 < V/J \lesssim 2$), this assumption is justified because the DW order is not expected there. This manipulation allows us to compare the obtained phase diagram with that of the GHM. The result is shown in Fig.5.

Next, the phase diagram *including a slow update of the variational parameter* ρ_{0a} in small V ($0 < V/J \lesssim 2$), is shown in Fig.A.1. Some quantities used for location of the phase boundaries are shown in Fig.A.1 (b), (c) and (d). This phase diagram also has a similar structure to that of the GHM for $g^2 > 0$. However, the phase diagram obtained by the MC of the GHM exhibits an enhancement of the SF, i.e., the Higgs phase, in the vicinity of $g^2 = 0$. As we explained above, this result comes from the fact that strong fluctuations of $\{\eta_a\}$ in that parameter region are taken into account properly in the GHM whereas not in the derivation of A_{eff} . Furthermore even for $V \rightarrow$ small, the phase transition lines in the two models do not coincide. Reason for this discrepancy is that in the Z_{EBH}^E in Eq.(A.6), the local density fluctuations $\{\rho_{0a}\}$ are taken into account. In fact, this hinders the effective hopping amplitude $J\sqrt{\rho_{0,a+1}\rho_{0a}}$ as the function

$f(x) = \sqrt{x(1-x)}$ has the maximum at $x = 1/2$.

Finally, Fig. A.2 exhibits a phase diagram *without rescaling by the mean density* ρ_0 . Here, we put, as an example of the large filling, $\rho_0 = 10$ (i.e., average occupation numbers of atoms per site is ten)[42]. The coupling constant J , U , and V are not rescaled by the mean density. We found that there are four phases, SF (superfluid), MI (Mott insulator), DW (density wave), and SS (supersolid). The DW state is recognized by the AF-type staggered configuration of the local density average $\{\rho_{0a}\}$. It is possible that both the quasi-long-range orders of the SF and the diagonal DW order coexist, indicating the supersolid (SS) state. The phase boundaries between SF(SS) and MI(DW) are determined by $\chi = \sum_\ell G_B(\ell)$. On the other hand, the boundaries between SF(MI) and MI(SS) is determined by the specific heat peak.

3. Gauge theoretical interpretation including inhomogeneity of density

Let us consider the physical meaning of each phase of the EBHM in the terminology of gauge theory [28]. The SF phase corresponds to the Higgs phase as the gauge fields $\theta_{r,\mu}$ has small fluctuations there. On the contrary, the MI corresponds to the confinement phase, as the boson density E_r , which is the electric field in the GHM, has small fluctuations in that phase; therefore, the vector potential $\theta_{r,\mu}$ fluctuates strongly in the MI. The above identification was verified in Sec. IV through the study on the real-time dynamics of the electric flux.

Next, we consider the DW and SS phases which appear for $g^2 \ll 0$. The DW phase has a definite density imbalance between even and odd sites., so that the density fluctuation from the mean density is basically small. Therefore, in terms of the gauge theory, the fluctuation of the electric field is small, which means that the DW phase follows the property of the confinement phase. We can say that the DW phase does not have substantial difference from the MI phase from gauge-theoretical point of view. In this sense, the SS state corresponds to the ordinary Higgs phase as the gauge fields $\theta_{r,\mu}$ have small fluctuations. In Fig. A.1 and Table II, we show the gauge-theoretical interpretation of the phase diagram of the EBHM.

TABLE II. Correspondence between the phases of EBHM and GHM. $\Delta\theta$ is the magnitude of fluctuations of atomic phase θ_a (vector potential $\theta_{r,1}$).

EBHM	U(1) GHM	$\Delta\theta$	ρ_{0a}
MI	Confinement	large	ρ_0 (homogeneous)
DW	Confinement	large	$\rho_{0,\text{even}} \neq \rho_{0,\text{odd}}$
SS	Higgs	small	$\rho_{0,\text{even}} \neq \rho_{0,\text{odd}}$
SF	Higgs	small	ρ_0 (homogeneous)

-
- [1] M. Noack, S. R. Manmana, AIP Conf. Proc. **789**, 93-163 (2005).
- [2] M. Troyer and U.-J. Wiese, Phys. Rev. Lett. **94**, 170201 (2005).
- [3] I. Bloch, J. Dalibard, and W. Zwerger, Rev. Mod. Phys. **80**, 885 (2008); M. Lewenstein, A. Sanpera, and V. Ahufinger, *Ultracold Atoms in Optical Lattices: Simulating Quantum Many-body Systems* (Oxford University Press, Oxford, 2012).
- [4] N. Goldman, G. Juzeliunas, P. Ohberg, and I. B. Spielman, Rep. Prog. Phys. **77** 126401 (2014).
- [5] For reviews, see, e.g., U.-J. Wiese, Ann. Phys. **525**, 777 (2013); E. Zohar, J. I. Cirac, and B. Reznik, Rep. Prog. Phys. **79**, 014401 (2016).
- [6] K. Kasamatsu, I. Ichinose, and T. Matsui, Phys. Rev. Lett. **111**, 115303 (2013).
- [7] Y. Kuno, K. Kasamatsu, Y. Takahashi, I. Ichinose, and T. Matsui, New J. Phys. **17**, 063005 (2015).
- [8] Y. Kuno, M. Sakane, K. Kasamatsu, I. Ichinose, and T. Matsui, Phys. Rev. A **94**, 063641 (2016).
- [9] E. Fradkin and S. H. Shenker, Phys. Rev. D **19**, 3682 (1979).
- [10] I. Ichinose and T. Matsui, Mod. Phys. Lett. B **28**, 1430012 (2014).
- [11] S. Baier, M. J. Mark, D. Petter, K. Aikawa, L. Chomaz, Z. Cai, M. Baranov, P. Zoller, and F. Ferlaino, Science **352**, 201 (2016).
- [12] O. Dutta, M. Gajda, P. Hauke, M. Lewenstein, D.-S. Luhmann, B. A. Malomed, Tomasz Sowinski, J. Zakrzewski Rep. Prog. Phys. **78**, 066001 (2015).
- [13] K. Wilson, Phys. Rev. D **10**, 2445 (1974); J. Kogut and L. Susskind, Phys. Rev. D **11**, 395 (1975).
- [14] S. Chandrasekharan and U. J. Wiese, Nucl. Phys. B **492**, 455 (1997).
- [15] Some further advantages of the present approach of identifying the phase of atomic variable to the U(1) gauge field over the quantum link-model is discussed in depth in Sec. I of Ref. [8].
- [16] M. Fattori, G. Roati, B. Deissler, C. D'Errico, M. Zaccanti, M. Jona-Lasinio, L. Santos, M. Inguscio, and G. Modugno, Phys. Rev. Lett. **101**, 190405 (2008); S. Müller, J. Billy, E. A. L. Henn, H. Kadau, A. Griesmaier, M. Jona-Lasinio, L. Santos, and T. Pfau, Phys. Rev. A **84**, 053601 (2011).
- [17] E. A. Martinez, C. A. Muschik, P. Schindler, D. Nigg, A. Erhard, M. Heyl, P. Hauke, M. Dalmonte, T. Monz, P. Zoller and R. Blatt, Nature(London), **534**, 516 (2016).
- [18] A. Bazavov, Y. Meurice, S.-W. Tsai, J. Unmuth-Yockey, and J. Zhang, Phys. Rev. D **92**, 076003 (2015).
- [19] V. L. Berezinskii, Sov. Phys. JETP **32**, 493(1971); *ibid* **34**,610 (1972); J. M. Kosterlitz and D. J. Thouless, J. Phys C**6**,1181(1973).
- [20] K. Adcox et al. (PHENIX Collaboration), Nucl.Phys.A **757**:184-283, (2005).
- [21] P.G. Kevrekidis, The Discrete Nonlinear Schrödinger Equation (Berlin: Springer) (2009).
- [22] T. Pichler, M. Dalmonte, E. Rico, P. Zoller, and S. Montagnero, Phys. Rev. X **6**, 011023 (2016).
- [23] A. Sinatra, C. Lobo, and Y. Castin, J. Phys. B At. Mol. Opt. Phys. **35**, 3599 (2002); A. Polkovnikov, Phys. Rev. A **68**, 053604 (2003); P. B. Blakie, a. S. Bradley, M. J. Davis, R. J. Ballagh, and C. W. Gardiner, Advances in Physics, **57**, 363 (2008).
- [24] T. Lahaye, C. Menotti, L. Santos, M. Lewenstein, and T. Pfau, Reports Prog. Phys. **72**, 126401 (2009); M. A. Baranov, M. Dalmonte, G. Pupillo, and P. Zoller, Chem. Rev. **112**, 5012 (2012).
- [25] S. Inouye, M. R. Andrews, J. Stenger, H.-J. Miesner, D. M. Stamper-Kurn, and W. Ketterle, Nature **392**, 151 (1998); C. Chin, et al. Rev. Mod. Phys. **82**, 1225 (2010)
- [26] This asymmetric XY model itself is related to a 1D quantum-rotor model and analyzed numerically in H. Zou, Y. Liu, C. Lai, J. Unmuth-Yockey, L. Yang, A. Bazavov, Z. Xie, T. Xiang, S. Chandrasekharan, S.-W. Tsai, Y. Meurice, Phys. Rev. A **90**, 063603 (2014).
- [27] W. Janke, Phys. Rev. B **55**, 3580 (1997).
- [28] See, for example, J. B. Kogut, Rev. Mod. Phys. **51**, 659 (1979).
- [29] For low density case, D. Rossini and R. Fazio, New J. Phys. **14**, 065012 (2012); G. G. Batrouni, V. G. Rousseau, R. T. Scalettar, and B. Gremaud, Phys. Rev. B **90**, 205123 (2014).
- [30] K. Kawaki, Y. Kuno, and I. Ichinose, Phys. Rev. B **95**, 195101 (2017).
- [31] L. P. Pitaevskii and S. Stringari, *Bose-Einstein Condensation* (Oxford University Press, Oxford, 2003); J. Rogel-Salazar, Eur J Phys **34**, 247 (2013).
- [32] F. Hebenstreit, J. Berges, and D. Gelfand, Phys. Rev. D **87**, 105006 (2013); V. Kasper, F.Hebenstreit, M.Oberthaler, and J.Berges, Phys. Lett. B **760**, 742 (2016).
- [33] P. Wurtz, T. Langen, T. Gericke, A. Koglbauer, and H. Ott, Phys. Rev. Lett. **103**, 080404 (2009).
- [34] J. Smit, Introduction to Quantum Fields on a Lattice (Cambridge Lecture Notes in Physics).
- [35] D. Banerjee, M. Dalmonte, M. Muller, E. Rico, P. Stebler, U.-J. Wiese, and P. Zoller, Phys. Rev. Lett. **109**, 175302 (2012).
- [36] J. Schwinger, Phys. Rev. **82**, 664 (1951).
- [37] Y. Kuno, K. Suzuki, and I. Ichinose, Phys. Rev. A **90**, 063620 (2014).
- [38] Strictly speaking, the correct expression is $\sum_{\eta_a \in \mathbf{Z}}$, which is replaced by the integral $\int_{-\infty}^{\infty} d\eta_a$ and the compactification
- [39] In the present discussion, we assume that a long-range order of the Ising-type fluctuations of η_a does not exist. If this long-range order exists, the system is in the density-wave. In this phase, the finite 'magnetization' exists.
- [40] This enhancement of the SF is actually observed by the SSE-quantum MC simulation of the EBHM at low fillings. See Ref. [30]
- [41] N. Metropolis, A. W. Rosenbluth, M. N. Rosenbluth, A. M. Teller, E. Teller, J. Chem. Phys. **21**, 1087 (1953).
- [42] In general, it is difficult to carry out a numerical simulation for large filling beyond mean-field theory due to enormous consumption of computer memory.